

Image Formation Using Fast Factorized Backprojection Based on Sub-Aperture and Sub-Image for General Bistatic Forward-Looking SAR with Arbitrary Motion

Dong Feng¹, Daoxiang An^{1, 2, *}, Xiaotao Huang^{1, 2}, and Tian Jin¹

Abstract—In this paper, a fast time domain imaging algorithm called bistatic forward-looking fast factorized backprojection algorithm (BF-FFBPA) based on sub-aperture and sub-image is proposed for general bistatic forward-looking synthetic aperture radar (BFSAR) with arbitrary motion. It can not only accurately dispose the large spatial variant range cell migrations and complicated motion errors, but also achieve high imaging efficiency. First, the imaging geometry and signal model are established, and the implementation of back projection algorithm (BPA) in the BFSAR imaging is given to provide a basis for the proposed BF-FFBPA. Then, considering motion errors, the more accurate requirements of splitting sub-aperture and sub-image in the BF-FFBPA is introduced based on the range error analysis to offer the tradeoff between the imaging quality and efficiency. Finally, the implementation and computational burden of the BF-FFBPA is provided and analyzed. Simulated results and evaluations are given to prove the correctness of the theory analysis and the validity of the proposed approach.

1. INTRODUCTION

Synthetic aperture radar (SAR) has gained wide attention these years [1–4], because it can not only get high resolution images of the observed area, but also work day and night under all weather conditions [4]. Therefore, it plays a significant role in both military and civilian fields. However, since the monostatic SAR working in the forward-looking mode has awful azimuth resolution and serious left-right ambiguity problem, its many applications, such as airplane navigation and terminal missile guidance, are greatly limited.

Bistatic SAR refers to SAR systems whose transmitter and receiver are mounted on the separate platforms, which is different from monostatic SAR with collocated transmitter and receiver. Compared to monostatic SAR, bistatic SAR has many advantages, such as obtaining different object scattering information, increasing system survival, and improving stealth in military. More importantly, bistatic SAR can improve azimuth resolution and avoid left-right ambiguity problem, and thereby can carry out the scene imaging in the forward direction. Different bistatic forward-looking SAR (BFSAR) experiments have been carried out these years [5–8], and a number of challenges have been shown in deploying BFSAR, such as synchronization, coherency and signal processing. The objective of this paper is focused on the signal processing in deploying BFSAR imaging, and imaging algorithm is the key point in the signal processing.

The existing imaging algorithms for BFSAR are divided into two categories: the frequency domain algorithms and the time domain algorithms. The frequency domain algorithms usually aim for minimizing processing time. This aim can lead to a number of limits such as bandwidth, integration

Received 17 January 2017, Accepted 27 March 2017, Scheduled 13 April 2017

* Corresponding author: Daoxiang An (daoxiangan@nudt.edu.cn).

¹ College of Electronic Science and Engineering, National University of Defense Technology, Changsha 410073, P. R. China.

² Collaborative Innovation Center of Information Sensing and Understanding, Xi'an 710077, P. R. China.

time, either interpolation or approximation in processing, and memory required by processing which may constrain the usage of the frequency domain algorithms. Recently, some modified frequency domain algorithms are applied on BFSAR imaging, such as the polar format algorithm (PFA) [9, 10], Omega-k algorithm [11], chirp scaling algorithm (CSA) [12], and nonlinear chirp scaling algorithm (NLCSA) [4]. However, the Omega-k algorithm and CSA are only available for the azimuth-invariant BFSAR [3]. Thus, they cannot always satisfy the imaging requirement for the general BFSAR geometry in practice. NLCSA has been used to implement the imaging for azimuth-variant BFSAR [4], but the approximations of handling the spatial-variant range cell migration and range-azimuth coupling may cause large phase errors in particular BFSAR cases.

Compared with the frequency domain algorithms, the back projection algorithm (BPA), which operates in the time domain, can work with almost all configurations of BFSAR in theory. However, the huge computational burden limits the application of the BPA. In order to solve the shortcoming of the BPA, some bistatic fast backprojection algorithms (Bi-FBPA) and bistatic fast factorized backprojection algorithms (Bi-FFBPA) have been proposed in [13–17], and they can be divided into two categories: one works with sub-aperture and polar grid processing [13–16], and the other works on a sub-aperture and sub-image basis [17]. In theory, the extensions of Bi-FBPA and Bi-FFBPA are totally valid for BFSAR without any modification. However, in some special cases of BFSAR, e.g., the centers of the polar grids are very close or even identical to one of the image coordinates, the performance of the Bi-FBPA and Bi-FFBPA which work with sub-aperture and polar grid processing may be very poor since there are difficulties in defining the polar grids [15]. But these difficulties are minimized in Bi-FBPA and Bi-FFBPA which work on a sub-aperture and sub-image basis. Besides, in the intermediate processing step, the Bi-FBPA and Bi-FFBPA which work with sub-aperture and polar grid processing use the polar grids, i.e., working with matrices, while the Bi-FBPA and Bi-FFBPA which work on a sub-aperture and sub-image basis use beams, i.e., working with vectors, hence, the computational burden required by the former may be heavier than the latter. Paper [17] presents the Bi-FBPA and Bi-FFBPA which work on a sub-aperture and sub-image basis, and the requirements of splitting sub-aperture and sub-image are given, but the sampling requirement of the beams was not given, and the requirements of splitting sub-aperture and sub-image are derived only for the linear track bistatic case. However, for the practical BFSAR acquisitions, the radar’s motion errors in the requirements of splitting sub-aperture and sub-image and the sampling requirement of the beams are essential details in the implementation of a precise BF-FFBPA.

Based on the previous work, this paper explores a BF-FFBPA based on sub-aperture and sub-image including the motion errors for the general BFSAR imaging. Firstly, the imaging geometry and signal model are established, and the implementation of BPA in the BFSAR imaging is given. Secondly, based on the range error analysis, the more accurate requirements of splitting sub-aperture and sub-image including motion errors are deduced, which offers the tradeoff between the imaging quality and efficiency. Thirdly, the method of beam forming is proposed, and the sampling requirement of the beams in the beam forming stage of implementation of BF-FFBPA is derived. Finally, the speed-up factor of the proposed BF-FFBPA with respect to BPA is derived.

The remainder of this paper is arranged as follows. Section 2 presents the BPA for general BFSAR with arbitrary motion based on the analysis of the imaging geometry and signal model. Section 3 gives details of the proposed BF-FFBPA. First, more accurate requirements of splitting sub-aperture and sub-image including motion errors are derived. Then, the implementation of the proposed BF-FFBPA is presented. Last but not the least, the computational burden is analyzed. Section 4 shows the simulated results and evaluations to prove the validity of the proposed approach, and Section 5 concludes this paper.

2. BPA FOR GENERAL BFSAR WITH ARBITRARY MOTION

2.1. Imaging Geometry and Signal Model

Since the platform’s speed is much less than the speed of light, the go-stop-go assumption is commonly used in the pulsed SAR [3, 13]. For the pulsed BFSAR case, transmitter and receiver are assumed stationary during the transmission and reception of the signal, and they move to the next position only

after the echo signal is received. Thus, the signal can be modeled as a function of two independent variables: fast time and slow time.

The imaging geometry of general BFSAR with arbitrary motion is shown in Fig. 1. The dashed straight lines l_1 and l_2 indicate the nominal flight tracks of the transmitter and receiver, while their actual flight tracks are solid curves l_3 and l_4 , respectively. The transmitter operates on the side-looking mode, while the receiver operates on the forward-looking mode. The positions of the transmitter and receiver at the slow time η are denoted as $(x_t(\eta), y_t(\eta), z_t(\eta))$ and $(x_r(\eta), y_r(\eta), z_r(\eta))$, respectively. $P(x, y, 0)$ is assumed to be an arbitrary target in the imaging scene. The transmitter and receiver are assumed to be perfectly synchronized. The travelling distance of a radar pulse radiated from a transmitter aperture impinging on this target and then reflected to a receiver aperture position at slow time η is calculated by

$$r(\eta; x, y) = r_t(\eta; x, y) + r_r(\eta; x, y) = \sqrt{(x_t(\eta) - x)^2 + (y_t(\eta) - y)^2 + (z_t(\eta))^2} + \sqrt{(x_r(\eta) - x)^2 + (y_r(\eta) - y)^2 + (z_r(\eta))^2} \quad (1)$$

If the transmitted signal is the linear frequency modulation (LFM) pulse signal, and its mathematic expression is $p(\tau) = w_r(\tau) \exp(j2\pi f_c \tau + j\pi K \tau^2)$, where τ is the fast time, $w_r(\cdot)$ the envelope of range, f_c the center frequency, and K the chirp rate, then, the received signal is

$$s(\tau, \eta) = \sigma_P w [\tau - r(\eta; x, y)/c] w_a(\eta - \eta_c) \exp \left[-j2\pi f_c r(\eta; x, y)/c + j\pi K (\tau - r(\eta; x, y)/c)^2 \right] \quad (2)$$

where σ_P is the reflectivity of the target P , c the speed of light, $w_a(\cdot)$ the envelope of azimuth, and η_c the synthetic aperture center time. Assume that the time bandwidth product (TBP) of the transmitted LFM pulse signal is very large and that the range envelope $w_r(\cdot)$ is a rectangle function. Then, the received signal after range compression can be approximated as

$$s_{rc}(\tau, \eta) \simeq \sigma_P \text{sinc} [B(\tau - r(\eta; x, y)/c)] w_a(\eta - \eta_c) \exp [-j2\pi f_c r(\eta; x, y)/c] \quad (3)$$

where B is the signal bandwidth, and the $\text{sinc}(\cdot)$ function is defined as

$$\text{sinc}(x) = \sin(\pi x)/(\pi x) \quad (4)$$

Due to the characteristic of azimuth space variance and serious range-azimuth coupling in the BFSAR imaging, it is quite difficult to reconstruct the imaging scene using the frequency domain algorithms. Different from the frequency domain algorithms, the time domain BPA is considered as a linear transformation from the echo signal into the reconstructed image, so it avoids the disposal of the spectrum of the BFSAR target and can be applied directly to the BFSAR imaging with perfect focusing performance.

2.2. BPA for General BFSAR with Arbitrary Motion

For the imaging geometry of general BFSAR with arbitrary motion shown in Fig. 1, assume that (x_p, y_q) is an arbitrary point in the discrete imaging scene grid. At slow time η , the travelling distance of a radar pulse radiated from a transmitter aperture impinging on the position (x_p, y_q) and then reflected to a receiver aperture position is calculated by

$$R_{pq}(\eta) = \sqrt{(x_t(\eta) - x_p)^2 + (y_t(\eta) - y_q)^2 + (z_t(\eta))^2} + \sqrt{(x_r(\eta) - x_p)^2 + (y_r(\eta) - y_q)^2 + (z_r(\eta))^2} \quad (5)$$

The position (x_p, y_q) is reconstructed by the superposition of backprojected radar echoes along the full synthetic aperture, and it is mathematically represented by the integral

$$h(x_p, y_q) = \int_{\eta_c - T/2}^{\eta_c + T/2} s_{rc}(R_{pq}(\eta)/c, \eta) \exp [j2\pi f_c R_{pq}(\eta)/c] d\eta \quad (6)$$

where T is the synthetic aperture time. An ellipsoidal mapping is the basic for the backprojection in BFSAR. The foci of the ellipsoid are defined by the actual aperture positions of the transmitter and receiver platforms, as shown in Fig. 1.

Due to the characteristic of point-by-point calculation, the practical application of BPA is limited by its heavy computational burden. Efficient time domain algorithms are urgently required to handle the BFSAR imaging precisely.

3. BF-FFBPA FOR GENERAL BFSAR WITH ARBITRARY MOTION

To reduce the computational burden of the BPA for general BFSAR imaging, a BF-FFBPA based on sub-aperture and sub-image for general BFSAR with arbitrary motion is presented in this section.

The proposed BF-FFBPA processes the BFSAR data on a sub-aperture and sub-image basis, i.e., local processing. This means that the complete transmitter and receiver apertures are split into a number of sub-apertures while the full reconstructed scene is segmented into a number of sub-images. Due to the local processing, the efficiency of image formation is significantly improved, whereas the range errors are caused in the processing stages, and the phase errors appear in the reconstructed image. The lower the number of sub-apertures and sub-images is, the shorter processing time BF-FFBPA requires, whereas the bigger phase error in the reconstructed image appears, so there is a tradeoff between the imaging efficiency and the imaging quality. Therefore, the requirements of splitting sub-aperture and sub-image play a significant role in the BF-FFBPA processing.

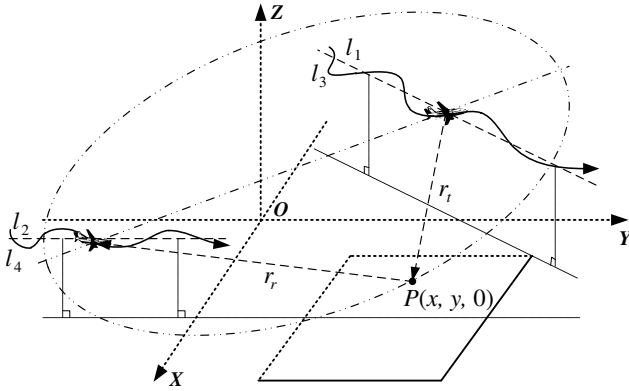


Figure 1. Imaging geometry with arbitrary motion of the general BFSAR.

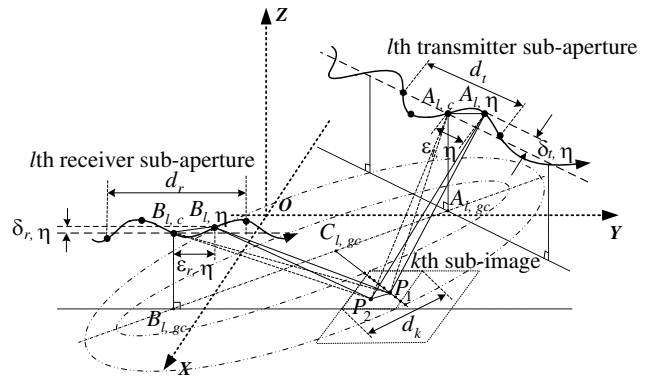


Figure 2. Range error analysis in BF-FFBPA for general BFSAR with arbitrary motion.

3.1. Requirements of Splitting Sub-Aperture and Sub-Image Considering Motion Errors

The proposed BF-FFBPA is able to handle nonlinear flight tracks of the transmitter and receiver as the derivation of the requirements of splitting sub-aperture and sub-image considers the motion errors. The motion errors here refer to the trajectory deviation errors.

In order to investigate the requirements of splitting sub-aperture and sub-image, we need to calculate the bistatic range error between the true travel distance of radar pulse and the processed travel distance. In the l th transmitter sub-aperture, the k th sub-image and the corresponding l th receiver sub-aperture, the bistatic range error between the true travel distance of radar pulse and the processed travel distance are depicted in Fig. 2. $A_{l,c}$ and $B_{l,c}$ are the positions of the l th transmitter and receiver sub-aperture center, respectively. Let d_t , d_r and d_k denote the length of the transmitter sub-aperture, the length of the receiver sub-aperture and the maximum dimension of the sub-image, respectively. $A_{l,\eta}$ and $B_{l,\eta}$ are the transmitter and receiver aperture positions at slow time η belonging to the l th sub-aperture, respectively. Let $\varepsilon_{t,\eta}$ be the distance between the positions $A_{l,c}$ and $A_{l,\eta}$ along the transmitter nominal track. $\delta_{t,\eta}$ is the across-track deviation of $A_{l,\eta}$ from the transmitter nominal track. Similarly, we use $\varepsilon_{r,\eta}$ to denote the distance between the positions $B_{l,c}$ and $B_{l,\eta}$ along the receiver nominal track, and $\delta_{r,\eta}$ to denote the across-track deviation of $B_{l,\eta}$ from the receiver nominal track. The length of the beam belonging to the k th sub-image is limited by two dotted-dashed ellipses in the ground. The foci of the ellipses are $A_{l,gc}$ and $B_{l,gc}$, which are the projections in the ground plane of $A_{l,c}$ and $B_{l,c}$, respectively. $C_{l,gc}$ is the center of the ellipses. P_1 is the position of the i th sample of the beam belonging to the k th sub-image. P_2 is an arbitrary image pixel in the k th sub-image whose value is mapped by the i th sample of the beam belonging to the k th sub-image.

Therefore, it is seen from Fig. 2 that the true travel distance of radar pulse radiated from the transmitter position $A_{l,\eta}$ impinging on the image pixel P_2 and then reflected to the receiver position

$B_{l,\eta}$ is $R = R_t + R_r$, where R_t and R_r indicate the lengths of the straight lines $A_{l,\eta}P_2$ and $B_{l,\eta}P_2$, respectively. However, the processed travel distance is $R' = R'_t + R'_r$, where R'_t and R'_r indicate the lengths of the straight lines $A_{l,\eta}P_1$ and $B_{l,\eta}P_1$, respectively. The difference between the true travel distance R and the processed travel distance R' causes a range error and thus a phase error in the reconstructed BFSAR image.

To calculate the range error in the BF-FFBPA for the general BFSAR with arbitrary motion, some auxiliary variables need to be introduced. Let ρ_t , σ_t , ρ_r , and σ_r be the lengths of the straight lines $A_{l,c}P_1$, $A_{l,c}P_2$, $B_{l,c}P_1$ and $B_{l,c}P_2$, respectively. Besides, we use β_t to denote the angle between the vector $\overrightarrow{A_{l,c}P_1}$ and the transmitter nominal motion direction, and $\Delta\beta_t$ to denote the angle between the vectors $\overrightarrow{A_{l,c}P_1}$ and $\overrightarrow{A_{l,c}P_2}$. Similarly, the angle between the vector $\overrightarrow{B_{l,c}P_1}$ and the receiver nominal motion direction is denoted by β_r , and the angle between the vectors $\overrightarrow{B_{l,c}P_1}$ and $\overrightarrow{B_{l,c}P_2}$ is denoted by $\Delta\beta_r$. Thus, the true travel distance R and the processed travel distance R' are determined by the law of cosine as

$$R = R_t + R_r = \sqrt{\sigma_t^2 + \varepsilon'_{t,\eta}{}^2 - 2\sigma_t\varepsilon'_{t,\eta} \cos(\beta_t + \Delta\beta_t + \varphi_t)} + \sqrt{\sigma_r^2 + \varepsilon'_{r,\eta}{}^2 - 2\sigma_r\varepsilon'_{r,\eta} \cos(\beta_r + \Delta\beta_r + \varphi_r)} \quad (7)$$

$$R' = R'_t + R'_r = \sqrt{\rho_t^2 + \varepsilon'_{t,\eta}{}^2 - 2\rho_t\varepsilon'_{t,\eta} \cos(\beta_t + \varphi_t)} + \sqrt{\rho_r^2 + \varepsilon'_{r,\eta}{}^2 - 2\rho_r\varepsilon'_{r,\eta} \cos(\beta_r + \varphi_r)} \quad (8)$$

where $\varepsilon'_{t,\eta} = \sqrt{\varepsilon_{t,\eta}^2 + \delta_{t,\eta}^2}$ and $\varepsilon'_{r,\eta} = \sqrt{\varepsilon_{r,\eta}^2 + \delta_{r,\eta}^2}$ indicate the lengths of the straight lines $A_{l,c}A_{l,\eta}$ and $B_{l,c}B_{l,\eta}$, respectively. φ_t and φ_r are the angles which are defined by $\varphi_t = \arctan(\delta_{t,\eta}/\varepsilon_{t,\eta})$ and $\varphi_r = \arctan(\delta_{r,\eta}/\varepsilon_{r,\eta})$, respectively. Applying the Taylor expansion for the square root terms on the right hand side of (7) and taking only the first two terms of the Taylor series into account, the true travel distance is then approximated by

$$R \approx \sigma_t + \sigma_r - \varepsilon'_{t,\eta} \cos(\beta_t + \Delta\beta_t + \varphi_t) - \varepsilon'_{r,\eta} \cos(\beta_r + \Delta\beta_r + \varphi_r) \quad (9)$$

Similarly, the processed travel distance can be approximated by

$$R' \approx \rho_t + \rho_r - \varepsilon'_{t,\eta} \cos(\beta_t + \varphi_t) - \varepsilon'_{r,\eta} \cos(\beta_r + \varphi_r) \quad (10)$$

According to the principle of ellipsoidal mapping, P_1 and P_2 are in the same ellipse whose foci are $A_{l,c}$ and $B_{l,c}$. Thus, due to the characteristics of an ellipse, the equation $\sigma_t + \sigma_r = \rho_t + \rho_r$ always holds true. Then, the range error is calculated as follows:

$$\begin{aligned} \Delta R &= \frac{(R - R')}{2 \cos(\alpha)} = \frac{\varepsilon'_{t,\eta} [\cos(\beta_t + \varphi_t) - \cos(\beta_t + \Delta\beta_t + \varphi_t)]}{2 \cos(\alpha)} + \frac{\varepsilon'_{r,\eta} [\cos(\beta_r + \varphi_r) - \cos(\beta_r + \Delta\beta_r + \varphi_r)]}{2 \cos(\alpha)} \\ &= \frac{\sqrt{\varepsilon_{t,\eta}^2 + \delta_{t,\eta}^2} \sin\left(\beta_t + \varphi_t + \frac{\Delta\beta_t}{2}\right) \sin\left(\frac{\Delta\beta_t}{2}\right)}{\cos(\alpha)} + \frac{\sqrt{\varepsilon_{r,\eta}^2 + \delta_{r,\eta}^2} \sin\left(\beta_r + \varphi_r + \frac{\Delta\beta_r}{2}\right) \sin\left(\frac{\Delta\beta_r}{2}\right)}{\cos(\alpha)} \end{aligned} \quad (11)$$

where α is half of the angle between the vectors $\overrightarrow{P_2A_{l,\eta}}$ and $\overrightarrow{P_2B_{l,\eta}}$. Assume that the maximum across-track deviations of transmitter and receiver from the nominal track along the full synthetic aperture are $\delta_{t,\max}$ and $\delta_{r,\max}$, respectively. Then, the following inequations hold true:

$$\begin{cases} 0 \leq \varepsilon_{t,\eta} \leq d_t/2 \\ 0 \leq \varepsilon_{r,\eta} \leq d_r/2 \\ 0 \leq \delta_{t,\eta} \leq \delta_{t,\max} \\ 0 \leq \delta_{r,\eta} \leq \delta_{r,\max} \\ \sin(\beta_t + \varphi_t + \Delta\beta_t/2) \leq 1 \\ \sin(\beta_r + \varphi_r + \Delta\beta_r/2) \leq 1 \end{cases} \quad (12)$$

Let ε_k , r_1 and r_2 be the lengths of the straight lines P_1P_2 , $A_{l,c}P_2$ and $B_{l,c}P_2$, respectively. Then we can see from Fig. 2 that

$$\begin{cases} \sin\left(\frac{\Delta\beta_t}{2}\right) \approx \frac{\varepsilon_k}{2r_1} \leq \frac{d_k}{4r_{1,\min}} \\ \sin\left(\frac{\Delta\beta_r}{2}\right) \approx \frac{\varepsilon_k}{2r_2} \leq \frac{d_k}{4r_{2,\min}} \end{cases} \quad (13)$$

where $r_{1,\min}$ and $r_{2,\min}$ are the minimum values of r_1 and r_2 along the full synthetic aperture, respectively. Combining Eqs. (11), (12) and (13), the upper bound of the range error can be represented as

$$\Delta R \leq \frac{d_k \sqrt{(d_t/2)^2 + \delta_{t,\max}^2}}{4r_{1,\min} \cos(\alpha)} + \frac{d_k \sqrt{(d_r/2)^2 + \delta_{r,\max}^2}}{4r_{2,\min} \cos(\alpha)} \quad (14)$$

Assume that the lengths of the full transmitter aperture and receiver aperture are S_t and S_r and that the size of imaging scene is $I_x \times I_y$. Then the number of sub-apertures is $L = S_t/d_t = S_r/d_r$, and the number of sub-images is $K = 2I_x I_y/d_k^2$. Therefore, the phase error appears in the reconstructed image caused by the range error can be represented as

$$\Delta\phi = \frac{2\pi}{\lambda} \Delta R \leq \frac{\pi \sqrt{2I_x I_y/K}}{4\lambda_{\min} \cos(\alpha)} \left[\frac{\sqrt{(S_t/L)^2 + 4\delta_{t,\max}^2}}{r_{1,\min}} + \frac{\sqrt{(S_r/L)^2 + 4\delta_{r,\max}^2}}{r_{2,\min}} \right] \quad (15)$$

where $\lambda_{\min} = c/(f_c + B/2)$ denotes the minimum wavelength of the signal. As shown in [3] and [17], if the maximum phase error is not bigger than $\pi/8$, the effect caused by the phase error can be neglected in the far-field SAR imaging. Thus, the splitting requirements of sub-aperture and sub-image can be represented as

$$K \geq \frac{8I_x I_y \left[\sqrt{(S_t/L)^2 + 4\delta_{t,\max}^2}/r_{1,\min} + \sqrt{(S_r/L)^2 + 4\delta_{r,\max}^2}/r_{2,\min} \right]^2}{\lambda_{\min}^2 \cos^2(\alpha)} \quad (16)$$

Equation (16) indicates that if the number of sub-apertures L is selected, the number of sub-images K should be selected no less than the right-hand side of Eq. (16).

3.2. Sampling Requirement of the Beams and Implementation

Reconstructing the BFSAR image by the proposed BF-FFBPA is divided into two stages, i.e., the beamforming stage and the backprojection stage. The method of beamforming in the first beamforming stage of the proposed BF-FFBPA is that all radar echoes after demodulation and range compression belonging to a sub-aperture are backprojected into the range center line in the ground plane belonging to a sub-image to form one beam. Take the l th sub-apertures and the k th sub-image shown in Fig. 2 for example, the range center line belonging to the k th sub-image is defined by the straight line crossing through the center of this sub-image and the center of the ellipse whose foci are the projections of the centers of the l th transmitter and receiver sub-apertures. In practice, the range center line is sampled to generate some discrete positions, and the beam is formed by backprojecting the radar echoes to these positions. The minimum length of the beam is limited by two dotted-dashed ellipses in the ground shown in Fig. 2.

In order to avoid aliasing in the beamforming, the sampling of the beam must satisfy requirement. Assume that the positions of the first and the last samples of the beam belonging to the l th sub-apertures, and the k th sub-image is denoted by P_{first} and P_{last} , respectively. Let N_b , Δb , and Δr be the number of samples that the beam consists of, the ground sampling interval of the beam, and the range sampling interval of the signal, respectively. Assume that the travel distances of a radar pulse radiated from the center of the l th transmitter sub-aperture impinging on the positions P_{first} and P_{last} , and then reflected to the corresponding center of the l th receiver sub-aperture are R_{first} and R_{end} , respectively. Let D be the length of the straight line $P_{\text{first}}P_{\text{last}}$. Thus, the following equations hold true:

$$\begin{cases} D = N_b \Delta b \\ R_{\text{end}} - R_{\text{first}} = N_b \Delta r \end{cases} \quad (17)$$

According to the Nyquist sampling theorem, the range sampling interval of the signal Δr must satisfy the requirement $\Delta r \leq c/B$, then the ground sampling interval of the beam Δb should satisfy the following requirement:

$$\Delta b \leq \frac{cD}{B(R_{\text{end}} - R_{\text{first}})} \quad (18)$$

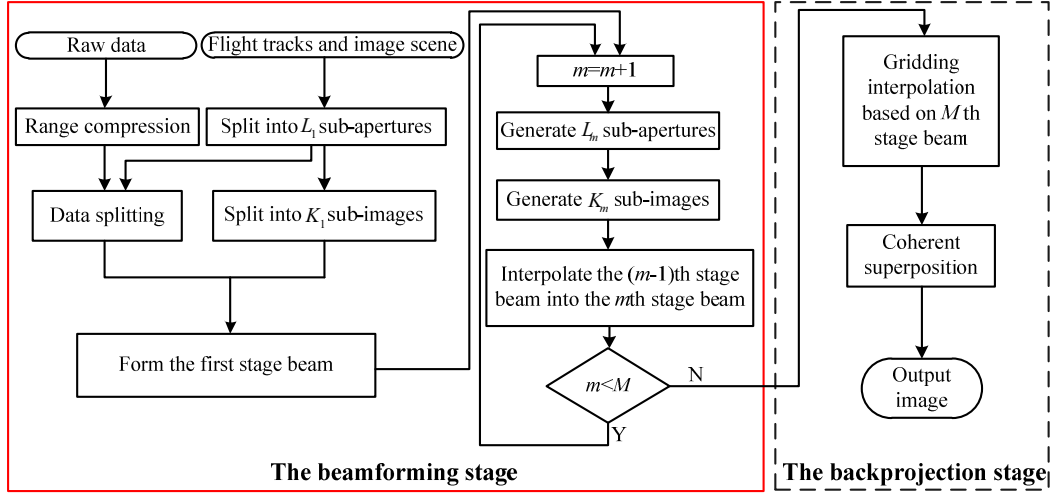


Figure 3. The flowchart of the implementation of the proposed BF-FFBPA.

Please note that the BF-FFBPA performs multiple beamforming stages before the backprojection stage. Fig. 3 shows the flowchart of the implementation of the proposed algorithm. The processing in the red solid rectangle is the beamforming stage, and the processing in the black dashed rectangle is the backprojection stage.

In the first beamforming stage, the full transmitter and receiver apertures are firstly split into L_1 sub-apertures which require a similar split of the range-compressed data at the same time, while the full reconstructed scene is segmented into K_1 sub-images according to Eq. (16). Take the l_1 th ($1 \leq l_1 \leq L_1$) sub-apertures and the k_1 th ($1 \leq k_1 \leq K_1$) sub-image for example. Assume that $(x_{l_1, k_1}, y_{l_1, k_1})$ is the position of an arbitrary sample of the beam belonging to the l_1 th sub-apertures and the k_1 th sub-image, then the value of this sample is determined by

$$b_{l_1, k_1}(x_{l_1, k_1}, y_{l_1, k_1}) = \int_{\eta_{l_1} - T_s/2}^{\eta_{l_1} + T_s/2} s_{rc}(R_{l_1, k_1}(\eta)/c, \eta) \exp[j2\pi f_c R_{l_1, k_1}(\eta)/c] d\eta \quad (19)$$

where η_{l_1} is the time instant corresponding to the l_1 th centers of the sub-apertures, and T_s is the integration time of the l_1 th sub-apertures. $R_{l_1, k_1}(\eta)$ is calculated by

$$R_{l_1, k_1}(\eta) = \sqrt{(x_t^{l_1}(\eta) - x_{l_1, k_1})^2 + (y_t^{l_1}(\eta) - y_{l_1, k_1})^2 + (z_t^{l_1}(\eta))^2} + \sqrt{(x_r^{l_1}(\eta) - x_{l_1, k_1})^2 + (y_r^{l_1}(\eta) - y_{l_1, k_1})^2 + (z_r^{l_1}(\eta))^2} \quad (20)$$

where $(x_t^{l_1}(\eta), y_t^{l_1}(\eta), z_t^{l_1}(\eta))$ and $(x_r^{l_1}(\eta), y_r^{l_1}(\eta), z_r^{l_1}(\eta))$ denote the transmitter and receiver aperture positions belonging to the l_1 th sub-apertures, respectively. Please note that y_{l_1, k_1} is the function of x_{l_1, k_1} in the range center line, i.e., $y_{l_1, k_1} = f(x_{l_1, k_1})$. Thus, $b_{l_1, k_1}(x_{l_1, k_1}, y_{l_1, k_1})$ can be represented as $b_{l_1, k_1}(x_{l_1, k_1}, y_{l_1, k_1}) = b_{l_1, k_1}(x_{l_1, k_1}, f(x_{l_1, k_1})) = b_{l_1, k_1}(x_{l_1, k_1})$. Assume that the travel distance of a radar pulse radiated from the center of the l_1 th transmitter sub-aperture impinging on the position $(x_{l_1, k_1}, y_{l_1, k_1})$ and then reflected to the center of the l_1 th receiver sub-aperture is denoted by $R_{l_1, k_1}^{l_1, c}(x_{l_1, k_1}, y_{l_1, k_1})$, which is calculated by

$$R_{l_1, k_1}^{l_1, c}(x_{l_1, k_1}, y_{l_1, k_1}) = \sqrt{(x_t^{l_1, c} - x_{l_1, k_1})^2 + (y_t^{l_1, c} - y_{l_1, k_1})^2 + (z_t^{l_1, c})^2} + \sqrt{(x_r^{l_1, c} - x_{l_1, k_1})^2 + (y_r^{l_1, c} - y_{l_1, k_1})^2 + (z_r^{l_1, c})^2} \quad (21)$$

where $(x_t^{l_1, c}, y_t^{l_1, c}, z_t^{l_1, c})$ and $(x_r^{l_1, c}, y_r^{l_1, c}, z_r^{l_1, c})$ are the positions of the centers of the l_1 th transmitter and receiver sub-apertures, respectively. Similarly, $R_{l_1, k_1}^{l_1, c}(x_{l_1, k_1}, y_{l_1, k_1})$ can be also represented as

$R_{l_1, k_1}^{l_1, c}(x_{l_1, k_1}, y_{l_1, k_1}) = R_{l_1, k_1}^{l_1, c}(x_{l_1, k_1})$. Therefore, x_{l_1, k_1} is the inverse function of $R_{l_1, k_1}^{l_1, c}$, i.e., $x_{l_1, k_1} = g(R_{l_1, k_1}^{l_1, c})$. Therefore, the beam formed in the l_1 th sub-apertures and k_1 th sub-image can be represented as

$$b_{l_1, k_1}(x_{l_1, k_1}, y_{l_1, k_1}) = b_{l_1, k_1}(R_{l_1, k_1}^{l_1, c}) \quad (22)$$

In the m th ($2 \leq m \leq M$, and M is the processing stages of beamforming) beamforming stage, the number of sub-apertures is combined into L_m , and the number of sub-images is changed into K_m . The new sets of beams in the m th stage are generated from the old sets of beams formed in the $(m-1)$ th beamforming stage. Assume that $(x_{l_m, k_m}, y_{l_m, k_m})$ is the position of an arbitrary sample of the beam belonging to the l_m th ($1 \leq l_m \leq L_m$) sub-apertures and the k_m th ($1 \leq k_m \leq K_m$) sub-image in the m th beamforming stage, and γ sub-apertures are combined into one sub-aperture each time, then the value of this sample is determined by

$$b_{l_m, k_m}(x_{l_m, k_m}, y_{l_m, k_m}) = b_{l_m, k_m}(R_{l_m, k_m}^{l_m, c}) = \sum_{l_{m-1}=1+(l_m-1)\gamma}^{l_m\gamma} b_{l_{m-1}, k_{m-1}}(R_{l_m, k_m}^{l_{m-1}, c}) \quad (23)$$

where

$$R_{l_m, k_m}^{l_m, c} = \sqrt{\left(x_t^{l_m, c} - x_{l_m, k_m}\right)^2 + \left(y_t^{l_m, c} - y_{l_m, k_m}\right)^2 + \left(z_t^{l_m, c}\right)^2} \\ + \sqrt{\left(x_r^{l_m, c} - x_{l_m, k_m}\right)^2 + \left(y_r^{l_m, c} - y_{l_m, k_m}\right)^2 + \left(z_r^{l_m, c}\right)^2} \quad (24)$$

and

$$R_{l_m, k_m}^{l_{m-1}, c} = \sqrt{\left(x_t^{l_{m-1}, c} - x_{l_m, k_m}\right)^2 + \left(y_t^{l_{m-1}, c} - y_{l_m, k_m}\right)^2 + \left(z_t^{l_{m-1}, c}\right)^2} \\ + \sqrt{\left(x_r^{l_{m-1}, c} - x_{l_m, k_m}\right)^2 + \left(y_r^{l_{m-1}, c} - y_{l_m, k_m}\right)^2 + \left(z_r^{l_{m-1}, c}\right)^2} \quad (25)$$

In Eq. (25), the coordinates $(x_t^{l_m, c}, y_t^{l_m, c}, z_t^{l_m, c})$ and $(x_r^{l_m, c}, y_r^{l_m, c}, z_r^{l_m, c})$ indicate the centers of the l_m th transmitter and receiver sub-apertures in the m th beamforming stage, respectively. In Eq. (26), the coordinates $(x_t^{l_{m-1}, c}, y_t^{l_{m-1}, c}, z_t^{l_{m-1}, c})$ and $(x_r^{l_{m-1}, c}, y_r^{l_{m-1}, c}, z_r^{l_{m-1}, c})$ indicate the centers of the l_{m-1} th transmitter and receiver sub-apertures in the $(m-1)$ th beamforming stage, respectively.

In the backprojection stage, the beams formed in the M th beamforming stage are backprojected into the imaging grid to reconstruct the final BFSAR image. The number of sub-apertures is L_M and the number of sub-images is K_M now. Take an arbitrary point in the k_M th ($1 \leq k_M \leq K_M$) sub-image grid for example. (x_{p, k_M}, y_{q, k_M}) is supposed to be the position of this point, then the value of this point after backprojecting is calculated by

$$h_{k_M}(x_{p, k_M}, y_{q, k_M}) = \sum_{l_M=1}^{L_M} b_{l_M, k_M}(R_{p, q, k_M}^{l_M, c}) \quad (26)$$

where

$$R_{p, q, k_M}^{l_M, c} = \sqrt{\left(x_t^{l_M, c} - x_{p, k_M}\right)^2 + \left(y_t^{l_M, c} - y_{q, k_M}\right)^2 + \left(z_t^{l_M, c}\right)^2} \\ + \sqrt{\left(x_r^{l_M, c} - x_{p, k_M}\right)^2 + \left(y_r^{l_M, c} - y_{q, k_M}\right)^2 + \left(z_r^{l_M, c}\right)^2} \quad (27)$$

The coordinates $(x_t^{l_M, c}, y_t^{l_M, c}, z_t^{l_M, c})$ and $(x_r^{l_M, c}, y_r^{l_M, c}, z_r^{l_M, c})$ indicate the centers of the l_M th transmitter and receiver sub-apertures, respectively. Therefore, the sampled version of the k_M th sub-image can be represented in the matrix form as follows:

$$H_{k_M} = \begin{bmatrix} h_{k_M}(x_{1, k_M}, y_{1, k_M}) & h_{k_M}(x_{1, k_M}, y_{2, k_M}) & \cdots \\ h_{k_M}(x_{2, k_M}, y_{1, k_M}) & \ddots & \vdots \\ \vdots & \cdots & \ddots \end{bmatrix} \quad (28)$$

The full BFSAR image is finally reconstructed by a union of all sub-images in a correct order.

3.3. Computational Burden

It is seen from the implementation of the proposed BF-FFBPA that the computational burden is mostly contributed by three parts, i.e., backprojecting the radar echoes into the range center lines, interpolating the old beams into the new beams, and interpolating the final beams into the image grids.

Assume that the number of transmitter and receiver aperture positions is N_l , and the imaging scene grid has the dimensions $N_x \times N_y$. In the first beamforming stage, the number of samples included in one beam is assumed to be N_b , then the computational burden of backprojecting the radar echoes into the range center lines C_1 is proportional to $L_1 K_1 \times (N_l/L_1) \times N_b$, i.e., $C_1 \propto K_1 N_l N_b$. In the m th beamforming stage, the new beams are interpolated from the old beams formed in the $(m - 1)$ th beamforming stage, so the computational burden of interpolating the $(m - 1)$ th beams into the m th beams is proportional to $\gamma N_b L_1 K_1$. Thus after M stages processing of beamforming, the computational burden C_2 can be represented as $C_2 \propto M \gamma N_b L_1 K_1$. In the backprojection stage, the beams formed in the M th beamforming stage are backprojected to the imaging scene grid, i.e., interpolating the final beams into the image grids. The needed number of operations can be represented as $C_3 \propto L_1 N_x N_y / \gamma^M$. Therefore, the total computational burden of the proposed BF-FFBPA is

$$C_{\text{BF-FFBPA}} = C_1 + C_2 + C_3 \propto K_1 N_l N_b + M \gamma N_b L_1 K_1 + L_1 N_x N_y / \gamma^M \quad (29)$$

Analogously, the computational burden of the BPA is given by

$$C_{\text{BPA}} \propto N_l N_x N_y \quad (30)$$

The speed-up factor of the proposed BF-FFBPA with respect to the BPA can be represented as

$$\kappa_{\text{BF-FFBPA}} = \frac{C_{\text{BPA}}}{C_{\text{BF-FFBPA}}} \propto \frac{N_l N_x N_y}{K_1 N_l N_b + M \gamma N_b L_1 K_1 + L_1 N_x N_y / \gamma^M} \quad (31)$$

Equation (16) shows that K_1 can be represented as the function of L_1 , thus the speed-up factor $\kappa_{\text{BF-FFBPA}}$ is proportional to the function of L_1 . Based on Eqs. (16) and (31), the variation trend of the speed-up factor $\kappa_{\text{BF-FFBPA}}$ with respect to L_1 is shown in Fig. 4. It is seen from Fig. 4 that the value of the speed-up factor $\kappa_{\text{BF-FFBPA}}$ changes along with the variety of the number of the sub-apertures L_1 , and the maximum speed-up factor can be obtained when L_1 lies on some location. That is to say, there is an optimal splitting of sub-aperture to make the imaging efficiency to be improved highest compared with the BPA.

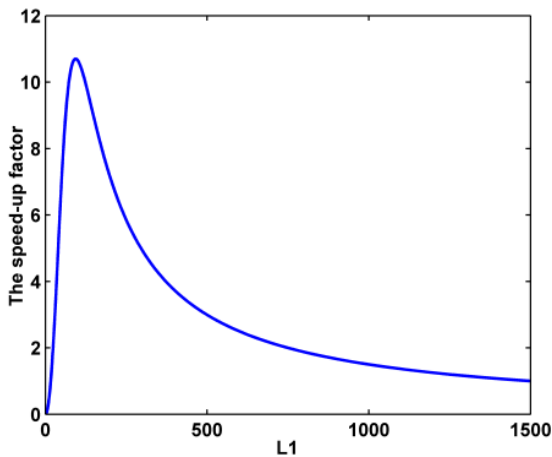


Figure 4. The variation trend of the speed-up factor with respect to L_1 .

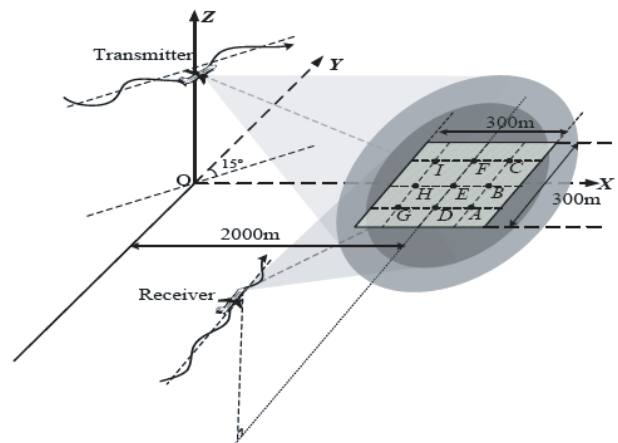


Figure 5. The imaging geometry of the simulated BFSAR imaging with arbitrary motion.

4. SIMULATION RESULTS AND EVALUATIONS

In order to prove the validity of the proposed BF-FFBPA, a comparative simulation experiment for the general BFSAR imaging is carried out in this section. The image reconstructed using BPA is used as a reference for comparison, since BPA can be seen as the most accurate imaging algorithm without any errors.

4.1. Arrangement

The simulation parameters are shown in Table 1, and the imaging geometry in this simulation is shown in Fig. 5. The transmitter works on the side-looking mode, and the angle between the nominal track of transmitter and Y -axis is 15° . The receiver works on the forward-looking mode, and the nominal track of receiver is parallel to Y -axis. The transmitter is assumed to be synchronized with the receiver perfectly. The same motion errors are added to the nominal flight tracks of the transmitter and receiver. The error added in X -axis is $\delta_x = 2 \sin(2\pi(0.3/3)\eta) + 0.1\eta$, the errors added in Y -axis is $\delta_y = 3 \sin(2\pi(0.8/3)\eta) + 0.2\eta$, and $\delta_z = 5 \sin(2\pi(0.5/3)\eta) + 0.3\eta$ is the errors added in Z -axis.

Table 1. Simulation parameters.

Parameters	Values	Parameters	Values
Center frequency (GHz)	10	Synthetic aperture time (s)	3
Signal bandwidth (MHz)	200	Transmitter nominal velocity (m/s)	40
Sampling frequency (MHz)	240	Transmitter nominal altitude (m)	2000
Pulse repetition frequency (Hz)	500	Receiver nominal velocity (m/s)	50
Pulse duration (μ s)	1	Receiver nominal altitude (m)	3500

The simulated ground scene consists of nine stationary point-like targets labeled as A-I in turn, which are equally spaced in an area of $300 \text{ m} \times 300 \text{ m}$ ($X \times Y$). The intervals of the targets in X and Y -directions are both 100 m, and the scene center position is (2000, 0, 0) m. The radar cross sections (RCS) of these targets are normalized to be 1 m^2 .

4.2. Imaging Results

To examine the proposed algorithm, we use the BPA and the proposed BF-FFBPA to reconstruct the same scene with the same simulated BFSAR data, and a comparative study between the results focused by the BPA and the proposed BF-FFBPA is used to prove the validity of the proposed algorithm.

The BPA can be implemented conveniently, but the implementation of the proposed BF-FFBPA needs to select the parameters carefully. The parameters here refer to the number of sub-apertures, number of sub-images and number of samples included in one beam in the beamforming stage, and the selections of these parameters for the BF-BBFPFA directly affect the imaging efficiency and quality.

From Fig. 4 we can know that there is an optimal splitting of sub-aperture which can make the speed-up factor arrive at maximum, and the optimal sub-aperture size in this simulation is calculated to be $L_1 = 93$. Thus, the number of sub-images can be selected to be $K_1 = 1521$ according to Eq. (16). In order to avoid aliasing in the beamforming, the number of samples included in one beam is selected to be $N_b = 128$.

Figure 6 shows the focused results of the point-like targets by the BPA and the proposed BF-FFBPA. The focused point-like targets shown in Figs. 6(b) and (c) are both inclined with a certain angle, which is believed to be dependent on the motion parameters of the radar platforms. Besides, the focused results of all point-like targets shown in Fig. 6(c) are very similar to the results shown in Fig. 6(b). Visually, there is no difference between the results focused by the BPA and those focused by the proposed BF-FFBPA, which indicates the validity of the proposed BF-FFBPA.

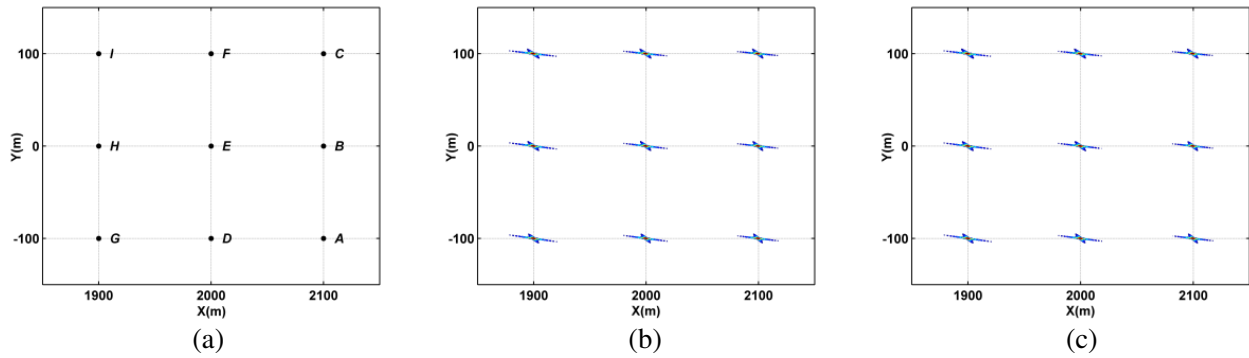


Figure 6. Focused results by different algorithms. (a) Distribution of targets. (b) BPA. (c) The proposed BF-FFBPA.

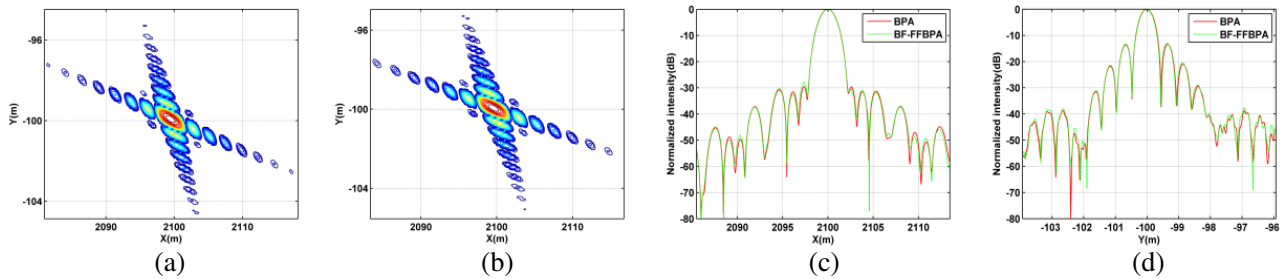


Figure 7. Target A. (a) Focused by BPA. (b) Focused by BF-FFBPA. (c) Cuts in X direction. (d) Cuts in Y direction.

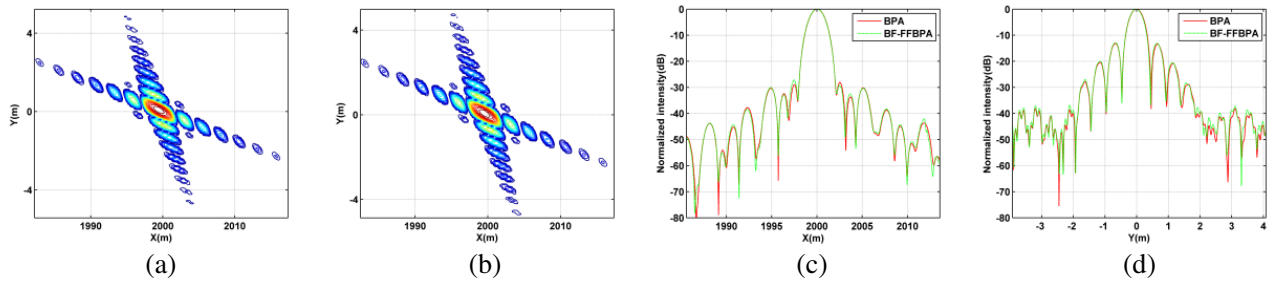


Figure 8. Target E. (a) Focused by BPA. (b) Focused by BF-FFBPA. (c) Cuts in X direction. (d) Cuts in Y direction.

4.3. Evaluation

To further evaluate the performance of the proposed algorithm, three focused point-like targets labeled as A, E and I are extracted from Fig. 6. The contours of targets A, E and I in the range $[-30, 0]$ dB are shown in Figs. 7, 8 and 9. Besides, the cuts containing the peak mainlobe in the X and Y directions of the considered point-like targets are also shown to compare the algorithms' performance. As observed from Figs. 7~9, the contours and cuts of the considered targets focused by the BPA and the proposed BF-FFBPA are very similar.

The half-power beamwidths (HPBW) of the considered targets A, E and I in both X and Y direction cuts are measured, and Table 2 shows the measured results. From Table 2, it is seen that the measured HPBWs obtained by the BPA and the proposed BF-FFBPA are almost identical, which allows us to predict that there is almost no loss in spatial resolutions due to phase errors caused by the

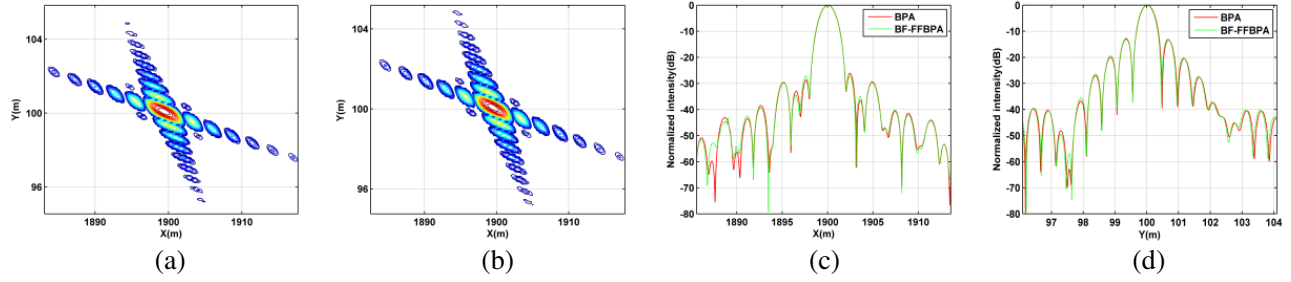


Figure 9. Target I. (a) Focused by BPA. (b) Focused by BF-FFBPA. (c) Cuts in X direction. (d) Cuts in Y direction.

Table 2. Measured HPBWs of the extracted targets.

Algorithms		Target A	Target E	Target I
BPA	X direction (m)	1.664	1.583	1.515
	Y direction (m)	0.392	0.392	0.392
The proposed BF-FFBPA	X direction (m)	1.664	1.583	1.502
	Y direction (m)	0.379	0.392	0.379

approximations in BF-FFBPA.

To prove the imaging efficiency of the proposed algorithm, the processing time of the proposed BF-FFBPA and BPA is measured in the Matlab R2013b on a computer with a 3.20 GHz Intel processor and 8.00 GB Random Access Memory (RAM). The average processing time of the BPA and the proposed BF-FFBPA are 1323 s and 138 s, respectively. Compared with BPA, the speed-up factor of the proposed BF-FFBPA is about 9.6. Therefore, a hint of the processing time reduction is clearly given by the measured results.

5. CONCLUSION

This paper presents a BF-FFBPA based on sub-aperture and sub-image for general BFSAR considering motion errors. It can not only accurately dispose the large spatial variant range cell migrations and complicated motion error, but also achieve high imaging efficiency. The imaging geometry and signal model are firstly established, based on which the difficulty of using frequency domain algorithm to reconstruct the BFSAR image is analyzed, and the implementation of BPA to reconstruct the BFSAR image is given. To reduce the computational burden, the BF-FFBPA based on sub-aperture and sub-image is successively proposed. The requirement of splitting sub-aperture and sub-image is deduced considering motion errors in the general BFSAR configuration, and the sampling requirement of the beams in the beamforming stages of the BF-FFBPA is given. Besides, the implementation of the proposed algorithm is presented, and the computational burden is discussed. Finally, the correctness of the theory analysis and validity of the proposed approach are proved by the simulations and evaluations.

ACKNOWLEDGMENT

This work was supported by the National Natural Science Foundation of China under Grants 61571447 and 61372161.

REFERENCES

1. Cumming, I. G. and F. H. Wong, *Digital Processing of Synthetic Aperture Radar Data: Algorithms and Implementation*, Artech House, Norwood, MA, USA, 2005.

2. An, D. X., Y. H. Li, X. T. Huang, X. Y. Li, and Z. M. Zhou, "Performance evaluation of frequency-domain algorithms for chirped low frequency UWB SAR data processing," *IEEE J. Sel. Topics Appl. Earth Observ.*, Vol. 7, No. 2, 678–690, 2014.
3. Xie, X. T., D. X. An, X. T. Huang, and Z. M. Zhou, "Fast time-domain imaging in elliptical polar coordinate for general bistatic VHF/UHF ultra-wideband SAR with arbitrary motion," *IEEE J. Sel. Topics Appl. Earth Observ.*, Vol. 8, No. 2, 879–895, 2014.
4. Chen, S., Y. Yuan, S. N. Zhang, H. C. Zhao, and Y. Chen, "A new imaging algorithm for forward-looking missile-borne bistatic SAR," *IEEE J. Sel. Topics Appl. Earth Observ.*, Vol. 9, No. 4, 1543–1552, 2016.
5. Yang, J. Y., Y. L. Huang, H. G. Yang, J. J. Wu, W. C. Li, Z. Y. Li, and X. B. Yang, "A first experiment of airborne bistatic forward-looking SAR preliminary results," *Proc IEEE Int. Geosci. Remote Sens. Symp. (IGARSS)*, 4202–4204, Melbourne, VIC, Australia, 2013.
6. Espeter, T., I. Walterscheid, J. Klare, A. R. Brenner, and J. H. G. Ender, "Bistatic forward-looking SAR: Results of a spaceborne-airborne experiment," *IEEE Geosci. Remote Sens. Lett.*, Vol. 8, No. 4, 765–768, 2011.
7. Wu, J. J., Y. L. Huang, J. Y. Yang, W. C. Li, and H. G. Yang, "First results of bistatic forward-looking SAR with stationary transmitter," *Proc IEEE Int. Geosci. Remote Sens. Symp. (IGARSS)*, 1223–1226, Vancouver, BC, Canada, 2011.
8. Walterscheid, I., A. R. Brenner, and J. Klare, "Radar imaging with very low grazing angles in a bistatic forward-looking configuration," *Proc IEEE Int. Geosci. Remote Sens. Symp. (IGARSS)*, 327–330, Munich, Germany, 2012.
9. Zhang, H. R., Y. Wang, and J. W. Li, "New applications of parameter-adjusting polar format algorithm in spotlight forward-looking bistatic SAR processing," *Proc. Asian Pacific Synth. Aperture Radar (APSAR)*, 384–387, Tsukuba, Japan, 2013.
10. Sun, J. P., Y. Lv, W. Hong, and S. Y. Mao, "The polar format imaging algorithm for forward-looking bistatic SAR," *Proc. Eur. Conf. Synth. Aperture Radar (EUSAR)*, 1–4, Friedrichshafen, Germany, 2008.
11. Shin, H. S. and J. T. Lim, "Omega-k algorithm for airborne forward-looking bistatic spotlight SAR imaging," *IEEE Geosci. Remote Sens. Lett.*, Vol. 6, No. 2, 312–316, 2009.
12. Wu, J. J., J. Y. Yang, Y. L. Huang, and H. G. Yang, "Focusing bistatic forward-looking SAR using chirp scaling algorithm," *Proc. IEEE Radar Conf. (RADAR)*, 1036–1039, Kansas, MO, USA, 2011.
13. Rodriguez-Cassola, M., P. Prats, G. Krieger, and A. Moreira, "Efficient time-domain image formation with precise topography accommodation for general bistatic SAR configurations," *IEEE Trans. Aerosp. Electron. Syst.*, Vol. 47, No. 4, 2949–2966, 2011.
14. Vu, V. T. and M. I. Pettersson, "Fast backprojection algorithms based on subapertures and local polar coordinates for general bistatic airborne SAR systems," *IEEE Trans. Geosci. Remote Sens.*, Vol. 54, No. 5, 2706–2712, 2016.
15. Vu, V. T., T. K. Sjögren, and M. I. Pettersson, "SAR imaging in ground plane using fast backprojection for mono- and bistatic cases," *Proc. IEEE Radar Conf. (RADAR)*, 0184–0189, Atlanta, GA, USA, 2012.
16. Shao, Y. F., R. Wang, Y. K. Deng, Y. Liu, R. P. Chen, G. Liu, and O. Loffeld, "Fast backprojection algorithm for bistatic SAR imaging," *IEEE Geosci. Remote Sens. Lett.*, Vol. 10, No. 5, 1080–1084, 2013.
17. Vu, V. T., T. K. Sjögren, and M. I. Pettersson, "Fast time-domain algorithms for UWB bistatic SAR processing," *IEEE Trans. Aerosp. Electron. Syst.*, Vol. 3, No. 49, 1982–1994, 2013.